minerals

MDPI

Article

Pyrite Trace-Element Signatures of Porphyry-Epithermal Systems in Xizang: Implications for Metallogenic Discrimination and Hydrothermal Evolution

Hongzhong Guan [1], Jiancuo Luosang [2,3,*], Lutong Gao [2] and Fuwei Xie [2]

[1] Tibet Zhongkai Holding Co., Ltd., Lhasa 850030, China; xizangreng@126.com
[2] College of Earth and Planetary Sciences, Chengdu University of Technology, Chengdu 610059, China; 18663098035@163.com (L.G.); xiefuwei19@cdut.edu.cn (F.X.)
[3] Tibet Xianglong Mining Co., Ltd., Xigaze 858500, China
* Correspondence: luosang8698@163.com

Abstract

The Zhunuo porphyry Cu deposit (2.9 Mt Cu @ 0.48%) in the Gangdese belt, southern Xizang, represents a key Miocene post-collisional system. This study integrates textural, major-, and trace-element analyses of pyrite from distinct alteration zones to unravel its hydrothermal evolution and metal precipitation mechanisms. Our study identifies four distinct pyrite types (Py1-Py4) that record sequential hydrothermal stages: main-stage Py2-Py3 formed at 354 ± 48 to 372 ± 43 °C (based on Se thermometry), corresponding to A and B vein formation, respectively, and late-stage Py4 crystallized at 231 ± 30 °C, coinciding with D-vein development. LA-ICP-MS data revealed pyrite contains diverse trace elements with concentrations mostly below 1000 ppm, showing distinct distribution patterns among different pyrite types (Py1-Py4). Elemental correlations revealed coupled behaviors (e.g., Au-As, Zn-Cd positive correlations; Mo-Sc negative correlation). Tellurium variability (7–82 ppm) records dynamic fO_2 fluctuations during system cooling. A comparative analysis of pyrite from the regional deposits (Xiongcun, Tiegelongnan, Bada, and Xiquheqiao) highlighted discriminative geochemical signatures: Zhunuo pyrite was enriched in Co-Bi-Ag-Pb (galena inclusions); Tiegelongnan exhibited the highest Cu but low Au-As; Xiquheqiao had the highest Au-As coupling; and Bada showed epithermal-type As enrichment. Partial Least Squares Discriminant Analysis (PLS-DA) identified Cu, As, and Bi as key discriminators for deposit types (VIP > 0.8), with post-collisional systems (Zhunuo and Xiquheqiao) showing intermediate Cu-Bi and elevated As versus arc-related deposits. This study establishes pyrite trace-element proxies (e.g., Se/Te, Co/Ni, and As-Bi-Pb) for reconstructing hydrothermal fluid evolution and proposes mineral-chemical indicators (Cu-As-Bi) to distinguish porphyry-epithermal systems in the Qinghai-Tibet Plateau. The results underscore pyrite's utility in decoding metallogenic processes and exploration targeting in collisional settings.

Keywords: pyrite; mineral chemistry; Zhunuo porphyry deposit; Xizang

check for updates

Academic Editor: Aleksei V. Travin

Received: 30 July 2025
Revised: 14 October 2025
Accepted: 15 October 2025
Published: 26 October 2025

Citation: Guan, H.; Luosang, J.; Gao, L.; Xie, F. Pyrite Trace-Element Signatures of Porphyry-Epithermal Systems in Xizang: Implications for Metallogenic Discrimination and Hydrothermal Evolution. *Minerals* **2025**, *15*, 1113. https://doi.org/10.3390/min15111113

Copyright: © 2025 by the authors. Licensee MDPI, Basel, Switzerland. This article is an open access article distributed under the terms and conditions of the Creative Commons Attribution (CC BY) license (https://creativecommons.org/licenses/by/4.0/).

1. Introduction

The giant Zhunuo porphyry deposit is located in the west part of the Gangdese belt in southern Xizang, containing 2.9 million tons of (Mt) Cu with an average grade of 0.48%. The discovery of this deposit significantly increases the exploration potential for porphyry deposit in the central-west part of the Gangdese belt [1,2]. As one of the most important

Miocene post-collisional porphyry Cu deposits in this belt, its hydrothermal evolution and related metal precipitation mechanism play an important role in understanding the formation of a giant porphyry deposit. Previous studies have discussed hydrothermal evolution by fluid inclusion and isotope studies, and conducted that Cu-Fe sulfides were precipitated during the chlorite ± muscovite alteration [3–6]. Meanwhile, in a porphyry system, the hydrothermal evolution is generally quite complex due to multiple mineralization pulses [7,8]. It is generally difficult to reveal the detailed hydrothermal evolution in a giant porphyry system using only fluid inclusion studies.

Recently, high spatial microanalysis of sulfides, using laser-ablation inductively coupled-plasma mass spectrometry (LA-ICP-MS), has been used to identify multiple fluid infiltration events [9,10]. Pyrite, the most widely distributed sulfide mineral [9], is a key indicator in diverse ore deposits. Its trace elements record ore-forming temperatures, environmental evolution, and denudation, aiding deep prospecting [11]. The enrichment of Au, Ag, and As preserves hydrothermal evolution and genetic signatures [11], making pyrite essential for studying fluid-to-metal enrichment processes. In porphyry systems, pyrite forms from magma to late mineralization stages, capturing the hydrothermal evolution [12–15]. In this contribution, we present textural results and major and trace element geochemistry of pyrite from different alteration zones to trace the hydrothermal evolution of the giant Zhunuo porphyry deposit in Xizang. In addition, we conducted a comparative study on the mineral chemistry of pyrite from different porphyry-epithermal deposits in the Qinghai-Tibet Plateau, establishing mineral chemical indicators for pyrite from different deposit types in this region.

2. Geologic Setting

The Gangdese belt is located in the south of the Lhasa terrane and hosts numerous porphyry-skarn Cu deposits, such as the Qulong [16], Jiama [17], Xiongcun [18], Bangpu [19], and Zhunuo deposits [6]. The Lhasa terrane can be subdivided into southern, central, and northern subterranes (Figure 1; [20]). The southern Lhasa subterrane, lying between the Luobadui-Milashan and Indus Yarlung fault systems, consists of extensive calc-alkaline magmatism, which has been interpreted to be related to the southward subduction of the Paleo-Tethys Ocean [21]. High positive $\varepsilon_{Hf}(t)$ of zircons from Jurassic magmatic rocks show the southern Lhasa subterrane is characterized by an oceanic basement and minor Late to Cretaceous volcano-sedimentary rocks [22,23]. The Gangdese batholith, which mainly comprises voluminous 243 to 8 Ma intrusions, dominates the southern Lhasa subterrane [24]. The Shiquan River-Nam Tso mélange zone separates the northern subterrane to the north and the central Lhasa subterrane to the south (Figure 1). The central Lhasa subterrane is characterized by a Precambrian crystalline basement and volcanic cover rocks [25]. The southward subduction of the Bangong-Nujiang ocean produced extensive calc-alkaline magmatism in the central Lhasa subterrane and intensive crustal growth that formed the northern Lhasa subterrnae (Figure 1; [25]).

The Zhunuo deposit is located near Angren, 200 km west of Xigaze (Figure 1). The detailed geology and geochronology of this deposit has been described by [5]. The Eocene volcanic rocks in the north of this deposit were components of the Pana Formation and were composed of rhyolite and andesite [5]. Three north-east trending reverse faults were distributed in the central of the Zhunuo deposit and cross-cut both Eocene volcanic rocks and intrusions. Furthermore, two north-west-trending inferred faults developed in the east and west of this deposit (Figure 2). Intrusions in this deposit included diorite porphyrite, dacite, lamprophyre, granodiorite, and quartz porphyry. Locally, breccias with outcrops less than 0.1 km^2 was observed within the quartz porphyry (Figure 2). Alteration on the surface was zoned and widely distributed in this deposit, including the potassic alteration in the southeast and the phyllic and propylitic alterations in the northwest (Figure 2).

Potassic alteration is characterized by the mineral assemblage of biotite + K-feldspar + quartz + amphibole ± sericite ± calcite ± anhydrite ± chlorite ± rutile, with metallic minerals including chalcopyrite + pyrite + molybdenite ± magnetite. Phyllic alteration, a medium-to-low temperature hydrothermal alteration type, occurred in both shallow and deep sections of the mining area. Its mineral assemblage consisted of sericite + quartz ± K-feldspar ± muscovite ± chlorite, accompanied by metallic minerals such as chalcopyrite + pyrite + molybdenite ± covellite ± bornite. Propylitic alteration zones were identified by the diagnostic epidote + chlorite assemblage, with alteration minerals including epidote + chlorite + sericite ± calcite ± anhydrite. Mineralization was weak in these zones, with sporadic molybdenite veins and disseminated pyrite/chalcopyrite observed.

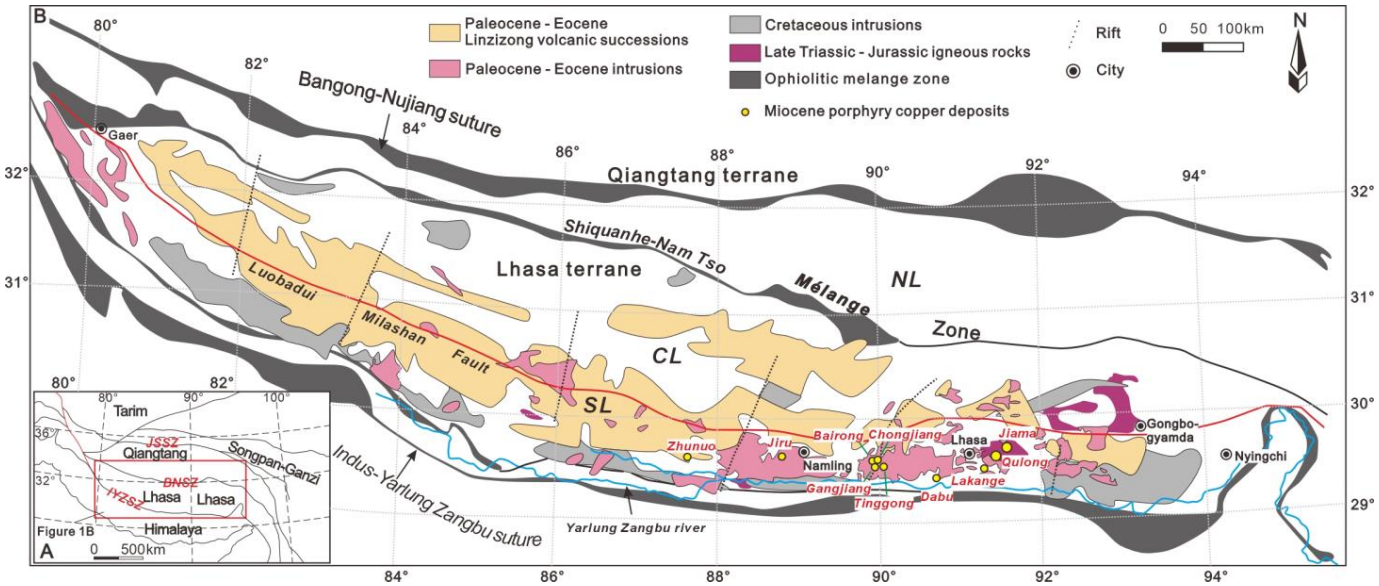


Figure 1. (**A**) Tectonic framework of the Tibetan Plateau (after [6]). (**B**) Geological map showing porphyry deposits in the Gandese Belt (after [6]). Abbreviations: CL: central Lhasa subterrane; SL: southern Lhasa subterrane; NL: northern Lhasa subterrane.

Veins were extensively developed in this deposit and could be divided into A, B, C, and D-type veins according to the nomenclature of [26]. The detailed vein characteristics have been described by [6]. Vein A was primarily associated with potassic-silicate alteration. Potassium feldspar occurred either as alteration halos around the vein or as an integral component of the vein itself. Quartz was predominantly granular, and the vein lacked symmetry. Vein B exhibited a symmetrical texture, with coarse-grained quartz and abundant sulfide mineralization (dominated by chalcopyrite and molybdenite, followed by pyrite). C veins were irregular and mainly composed of minerals such as chalcopyrite and chalcopyrite. Vein D appeared straight and narrow, displaying thin white sericite alteration halos. Sulfides within this vein were predominantly pyrite, with minimal chalcopyrite.

Orebodies in the Zhunuo deposit occurred with an irregular lens shape and were developed within the monzogranite porphyry. Spatially, orebodies developed within the potassic alteration zone and were overprinted by the phyllic alteration. Chalcopyrite and bornite dominated the economic Cu-Fe sulfides in this deposit. Molybdenite mostly occurred as flaky or scaly aggregates distributed in the B veins. Pyrite was also widely distributed in this deposit, especially within the D veins. Overall, the Cu grade had a positive correlation with the abundance of A and B veins. A decreasing trend of Cu grade with distance could be observed from the center of the monzogranite porphyry.

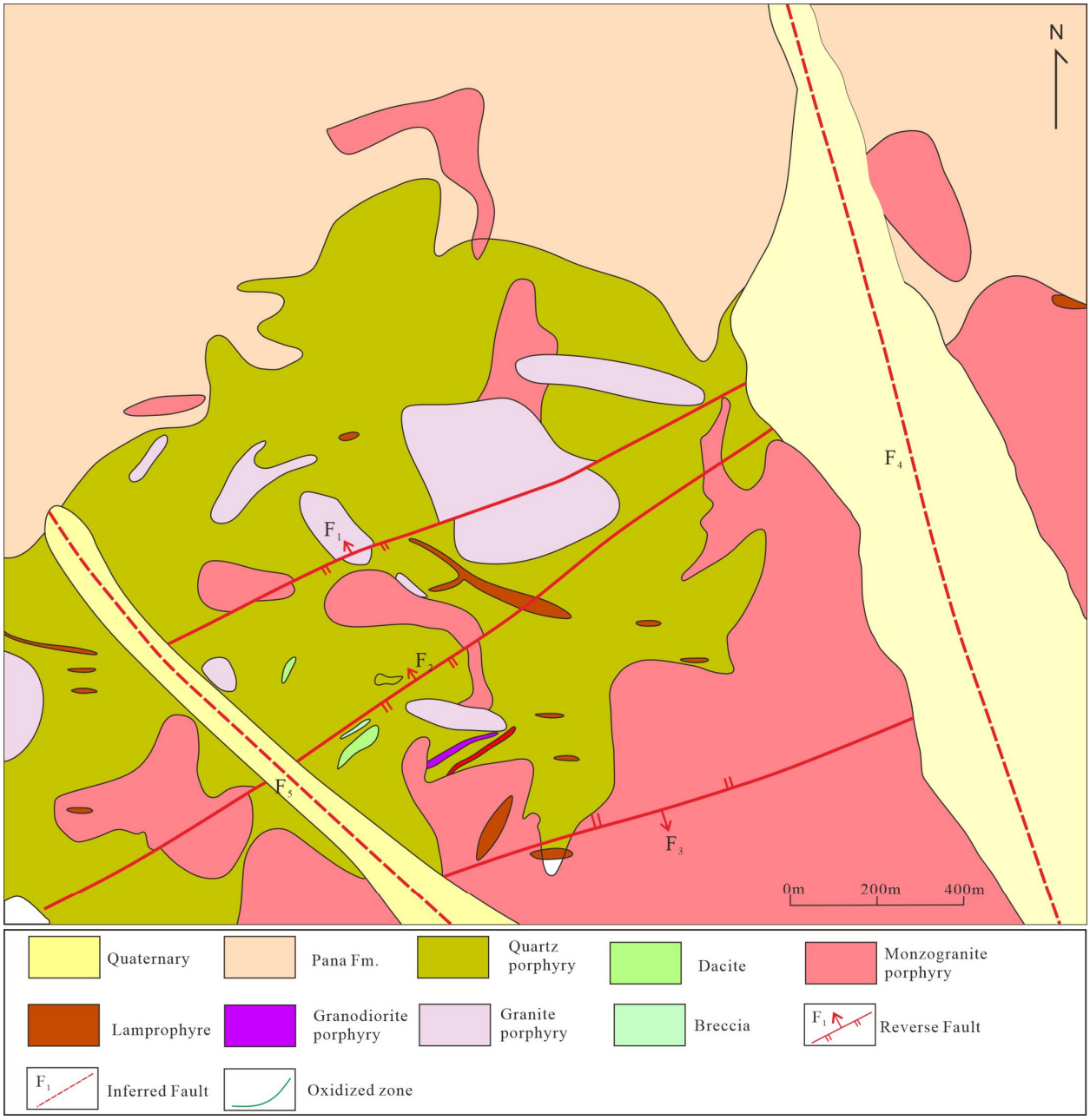


Figure 2. Geological map of the Zhuonuo deposit.

3. Sampling and Analytical Methods

Samples were collected from the Zhunuo deposit. Three types of pyrite were found in 13 samples (Table 1). The sampling borehole locations are shown in Figure 2. Thin sections were prepared for SEM characterization and LA-ICP-MS geochemical quantification. In addition, we collected pyrite mineral chemistry data from copper-gold deposits, including the Xiongcun porphyry deposit in an island arc setting [27], the Tiegelongnan porphyry-epithermal deposit in a continental margin arc setting [28], and the Bada epithermal deposit [29] and Xiquheqiao deposit [30] in a post-collisional setting.

Element analyses of pyrites in thin sections were conducted by LA-ICP-MS at Nanjing FocuMS Technology Co., Ltd. Teledyne Cetac Technologies Analyte Excite laser-ablation system (Bozeman, MT, USA) and Agilent Technologies 7700× quadrupole ICP-MS (Hachioji, Tokyo, Japan) were combined for the experiments. The 193 nm ArF excimer laser, homogenized by a set of beam delivery systems, was focused on the sulfide surface with

fluence of 3.0 J/cm^2. Each acquisition incorporated 20 s background (gas blank), followed by spot diameter of 40 um at a 5 Hz repetition rate for 40 s. Helium(370 mL/min) was applied as carrier gas to efficiently transport aerosol out of the ablation cell, and was mixed with argon (~1.15 L/min) via the T-connector before entering the ICP torch. USGS polymetal sulfide-pressed pellet MASS-1 and synthetic basaltic glasses GSE-1G were combined for external calibration. Quantitative calculation of the element contents was performed using the "internal standard-free matrix normalization method". The measured isotope species included: ^{34}S, ^{57}Fe, ^{65}Cu, ^{66}Zn, ^{95}Mo, ^{23}Na, ^{25}Mg, ^{27}Al, ^{29}Si, ^{31}P, ^{39}K, ^{42}Ca, ^{45}Sc, ^{49}Ti, ^{51}V, ^{53}Cr, ^{55}Mn, ^{59}Co, ^{60}Ni, ^{71}Ga, ^{72}Ge, ^{75}As, ^{78}Se, ^{85}Rb, ^{88}Sr, ^{89}Y, ^{109}Ag, ^{111}Cd, ^{115}In, ^{118}Sn, ^{121}Sb, ^{125}Te, ^{133}Cs, ^{137}Ba, ^{183}W, ^{197}Au, ^{205}Tl, ^{209}Bi, ^{232}Th, $^{206/207/208}$Pb, and ^{238}U. The offline processing of analytical data was performed using ICPMSDataCal software 10.1. The analysis results along with their uncertainties and detection limits are presented in Tables S1 and S2.

Table 1. Classification of pyrite types in selected samples with their associated alteration/vein types and characteristics.

Types of Pyrite	Textural Occurrence	Associated Veins or Alterations	Alteration or Vein Mineral Assemblage	Formation Temperature Based on Inclusions	References
Py1	Dissemination	Phyllic alteration	Sericite, pyrite, quartz, K-feldspar, muscovite, and chlorite		
Py2	Dissemination	Phyllic and potassic alteration	Biotite, K-feldspar, quartz, amphibole, sericite, calcite, anhydrite, chlorite, rutile, and magnetite		
Py3	Predominantly vein-type with local dissemination	Phyllic alteration, A-vein, and C-vein	Quartz–pyrite–chalcopyrite veins, quartz–muscovite–pyrite–chalcopyrite veins, pyrite–chalcopyrite veins	340 °C to 400 °C	[6]
Py4	Vein	D-vein	Quartz-pyrite or pyrite veins	220 °C to 330 °C	[6]

Partial Least Squares Discriminant Analysis (PLS-DA) multivariate statistics: Pyrite trace element compositions were analyzed using Partial Least Squares Discriminant Analysis (PLS-DA), a supervised multivariate statistical method designed to classify labeled geochemical data [31,32]. PLS-DA has been widely applied in mineral geochemistry to distinguish various mineral phases, including iron oxides, tourmaline, native gold, rutile, chalcopyrite, and scheelite, thereby demonstrating its broad applicability and effectiveness [33–36].

Prior to analysis, the dataset was pre-processed to address censored values (i.e., those below detection limits). These were imputed using the robCompositions package in R 4.5.1, specifically employing the impKNNa function, which estimates missing values based on the Aitchison distance using k-nearest neighbors. Elements for which more than 40% of the data fell below detection limits were excluded from further analysis. The imputed data were then transformed using the centered log-ratio (clr) transformation, which provides a symmetric and orthonormal basis for compositional data [37].

PLS-DA score scatter plots (t-scores) were used to distinguish elemental associations within sample groups, while the corresponding loading plots (q_v*) revealed correlations among elements and their contribution to group separation. Elements plotting near one another in both loading and score plots exhibited positive correlations, whereas those in opposing quadrants were negatively correlated. Data points situated near the origin in both plots represent compositions close to the dataset mean and, therefore, are less effectively discriminated by the PLS-DA model.

Score contribution plots illustrate the relative enrichment or depletion of elements within specific sample groups, showing whether elemental concentrations are higher or lower compared to the overall mean. The Variable Importance in Projection (VIP) scores

were also calculated to evaluate the influence of each element on group classification, with values greater than 0.8 considered significant for the model.

4. Pyrite Mineralogy and Textures

Pyrite is the most abundant sulfide mineral in the Zhunuo copper deposit, with an average concentration of approximately 0.64 wt.% in the ore. It predominantly occurs in two modes: vein-type (Figure 3A–C) and disseminated (Figure 3D–F). Pyrite-bearing veins include quartz–pyrite–chalcopyrite (A vein, Figure 3A), quartz–muscovite–pyrite–chalcopyrite (A vein, Figure 3B), and pyrite–chalcopyrite (C vein, Figure 3C) assemblages, with vein thicknesses ranging from 0.2 to 2 cm. Microscopically, disseminated pyrite is mainly characterized by anhedral granular and replacement textures, although euhedral granular, zoned, and cataclastic textures are also locally observed.

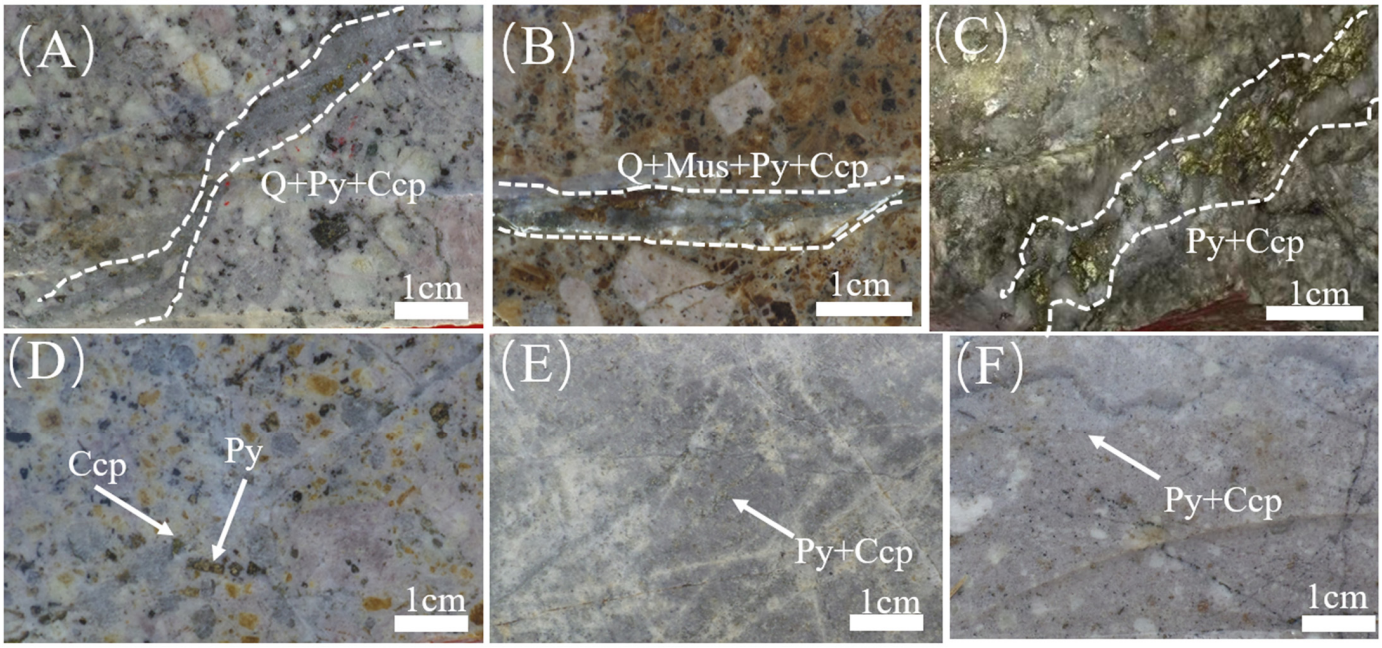


Figure 3. Macro-geological characteristics of the Zhunuo copper deposit. (**A**) Quartz-pyrite-chalcopyrite veins; (**B**) Chalcopyrite-pyrite veins; (**C**) Quartz-muscovite-chalcopyrite-pyrite veins; (**D**) Disseminated euhedral pyrite in weakly sericitized alteration zone; (**E**) Disseminated pyrite and chalcopyrite in strongly sericitized alteration; (**F**) Disseminated pyrite and chalcopyrite in silicified-weakly sericitized alteration zone.

Detailed core logging, petrographic analysis, and paragenetic relationships reveal the presence of three distinct types of pyrite in the Zhunuo deposit. Type 1 (Py1) represents subhedral pyrite disseminated in the matrix, with some pentagonal dodecahedral pyrite grains exhibiting features of brittle deformation (Figure 4A). Type 2 (Py2) occurs as disseminated pyrite within silicified zones exhibiting weak to intense sericitic alteration. This pyrite type is completely replaced by chalcopyrite (Figure 4B–D) and locally coexists with sphalerite (Figure 4D). Type 3 (Py3) occurs both as vein-hosted pyrite in sericitically altered zones with chalcopyrite, showing semi-euhedral to euhedral granular morphologies (Figure 4E,F), and as disseminated semi-euhedral to euhedral pyrite along biotite phenocryst margins or in the groundmass. Some Py3 grains contain Ti-rich sulfide or galena inclusions (Figure 4G,H), although most are partially to fully replaced by chalcopyrite (Figure 4H). Type 4 (Py4) consists exclusively of euhedral granular pyrite and is also replaced by chalcopyrite (Figure 4I).

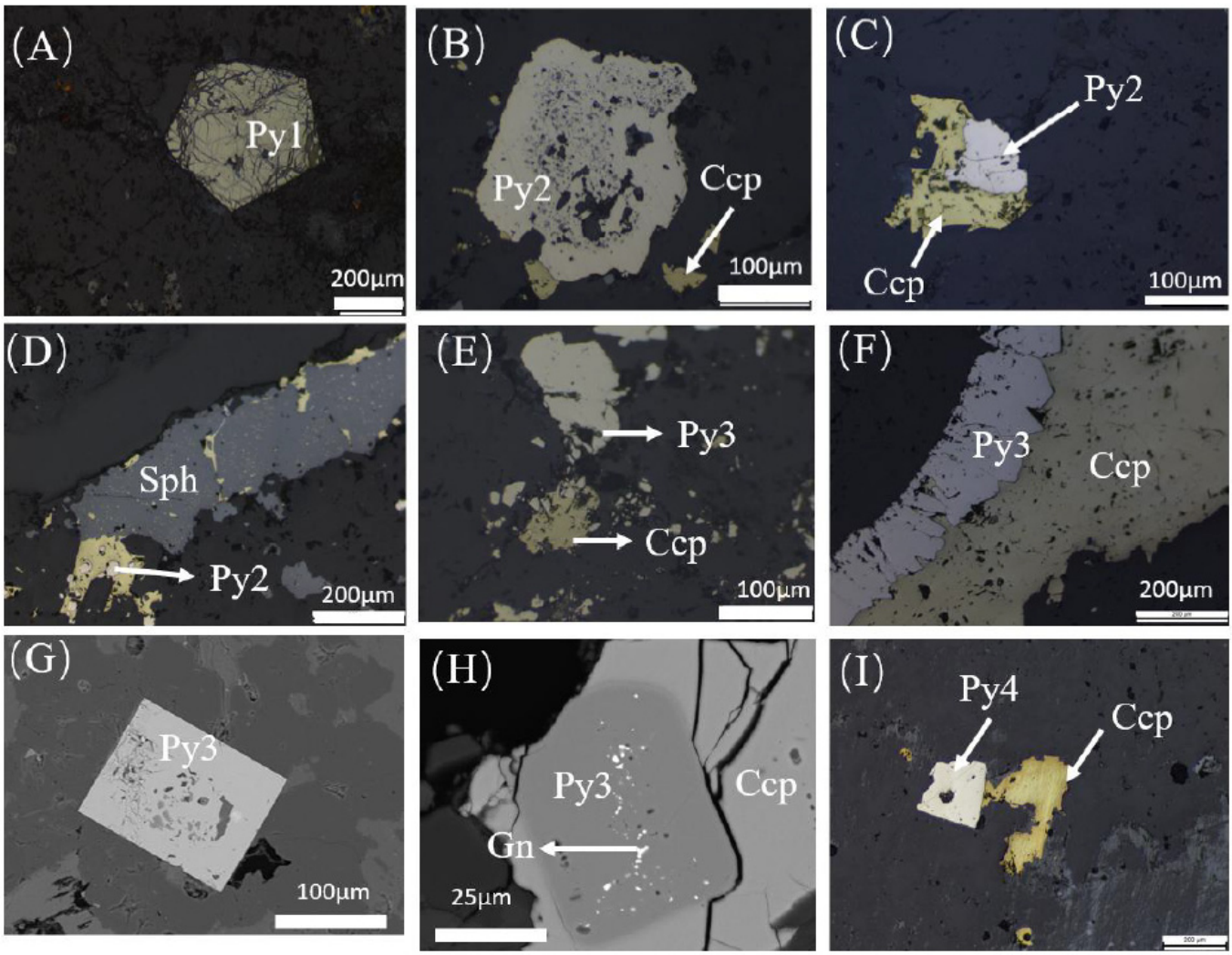


Figure 4. (**A**) Sample ZK404-138.7: Cataclastic euhedral Py1 in strong sericitic-altered zone. (**B**) Sample ZK2104-345: Coexisting Py2 (smooth edges, porous core) and chalcopyrite in a silicified-weak sericitic alteration. (**C**) Sample ZK7A08-237.35: Anhedral Py2 coexisting with chalcopyrite in weak sericitic alteration. (**D**) Sample ZK2307-195.2: Py3 replaced by chalcopyrite (coexisting with sphalerite) in a strong sericitic alteration. (**E**) Sample 7A04-223.4: Abundant Py3 with minor chalcopyrite in quartz-sulfide vein. (**F**) Sample ZK1106-505.4: Quartz-chalcopyrite + Py3 vein. (**G**) Sample ZK7A04-223.4: Disseminated euhedral Py3 in porphyry. (**H**) Sample 7A03-292.7: Matrix-hosted chalcopyrite coexisting with Py3 (containing galena inclusions) in a weak sericitic alteration. (**I**) Sample ZK7A03-292.7: Py4 associated with chalcopyrite.

5. Results

Pyrite hosts a large variety of trace elements, with the concentration of most elements being below 1000 ppm (Figure 5). Lead, Co and Ni have relatively higher concentration, with average contents slightly over 100 ppm. Concentration of Cu, As, Se, and Bi are lower with average values between 10 and 100 ppm. The average concentrations of Te, Cr, Zn, Ag and Ge are even lower ranging between 1 and 10 ppm. Other elements have low concentrations below 1 ppm (Figure 5), and many analyses are below detection limit (Table S1).

The concentration of elements varied among different groups of pyrite (Figure 6). Py3 had slightly higher Au contents compared to other groups in general, although the contents were still low, mostly less than 1 ppm (Figure 6A). Arsenic showed a similar trend to Au, but higher concentrations were obtained in Py2, with values close to 100 ppm (Figure 6B). Py4 had a more concentrated range of Au and As, whereas data for Py2 were more scattered

with a wider box range for Au and As. Py4 had the highest content of Cu, Cd, and Ni (Figure 6A,E,F,H), compared with all of the other elements. Sc concentrations were also higher in Py2. Py3 had the highest contents of Bi and Mo relative to the other samples (Figure 6D). In contrast, Py1 had the lowest concentration of most elements, including As, Ag, Bi, Cu, Ni, Se, Sb, Te, and Zn (Figure 6B–E,H,K,M,N,P). Py3 had the highest concentrations of Sn, Sb, and Zn (Figure 6L,M) for all pyrite samples.

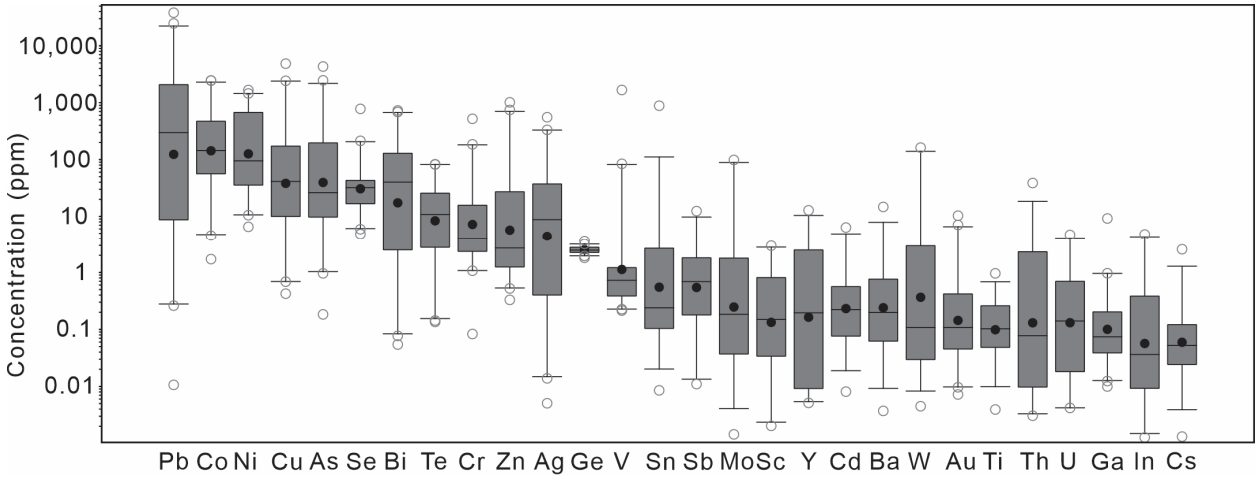


Figure 5. Trace element concentration of pyrite from the Zhunuo porphyry deposit. Boxes represent 25th to 75th percentiles; whiskers show 5% and 95% values; circles outside the boxes represent outliers (the top and bottom 5% of data); black circles are trimmed mean values (mean of values within top and bottom of whiskers); middle lines are median values.

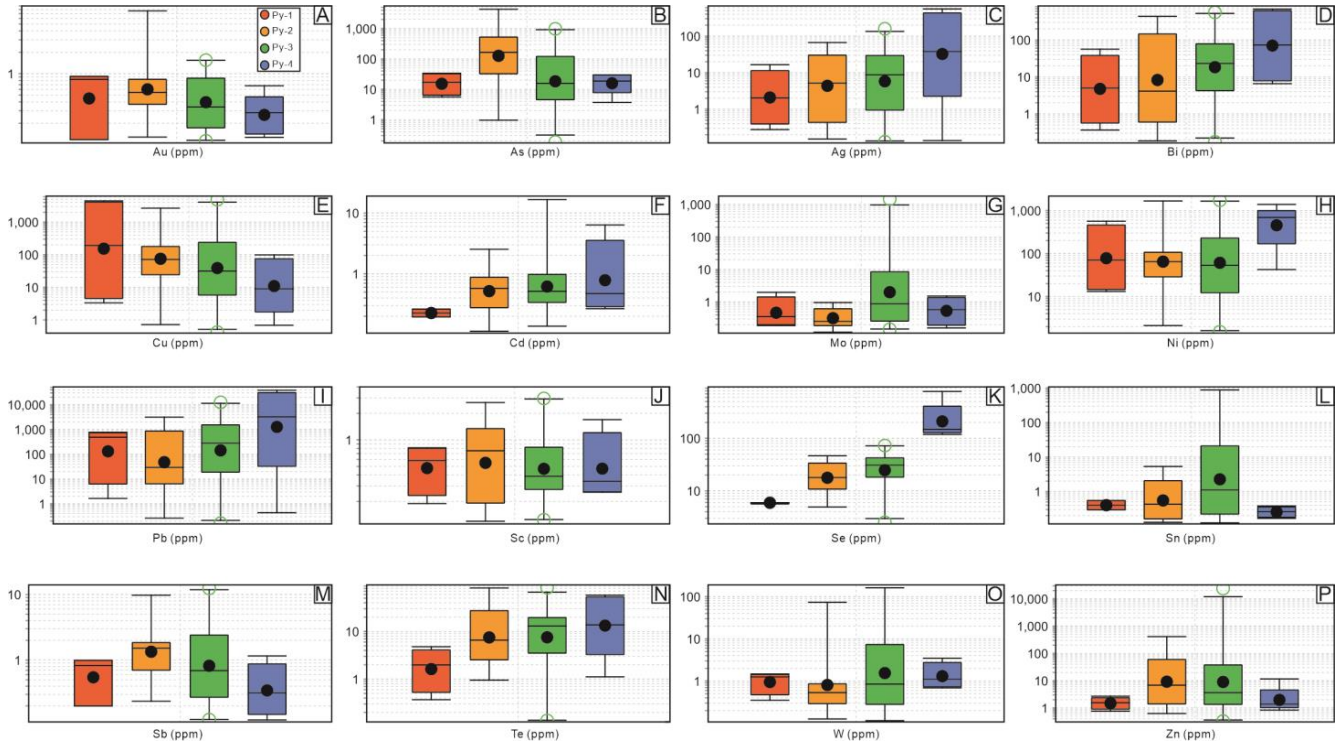


Figure 6. Box-whisker diagrams of key trace elements in various groups of pyrite from the Zhunuo deposit. Box-whisker information is the same as that in Figure 5.

Some elements showed a close correlation between one another. For example, Au had a positive correlation with As (Figure 7A), suggesting they might be incorporated into pyrite via the same process. Other coupled element groups included Zn and Cd (Figure 7B),

Sb and Bi (Figure 7C), Te and Bi (Figure 7D), and Se and Bi (Figure 7E). However, for the Sb and Bi, and Te and Bi pairs, some Py2 plots did not show a positive correlation. Conversely, Mo and Sc displayed a negative correlation (Figure 7F), suggesting competitive substitution during their incorporation into the pyrite lattice.

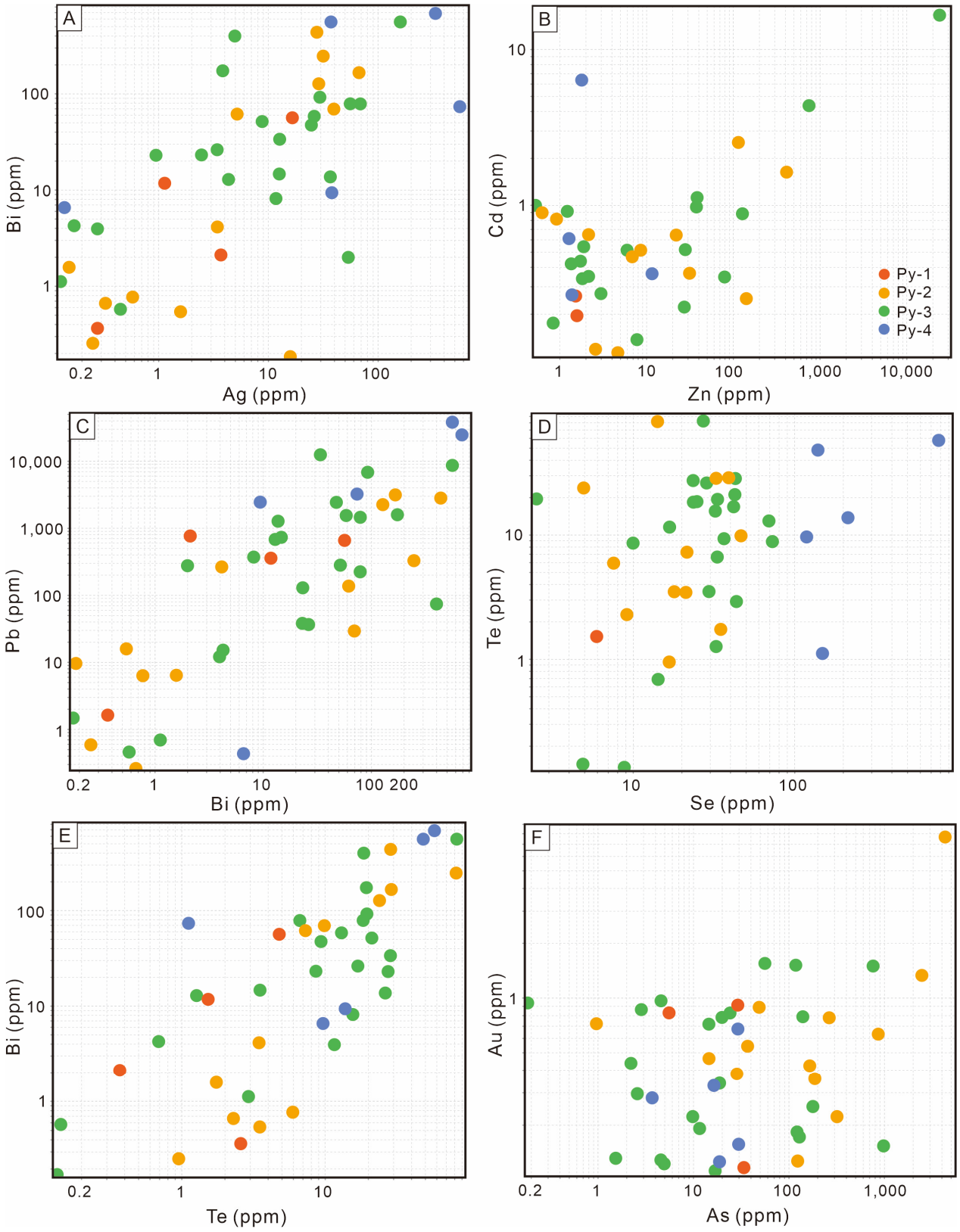


Figure 7. Biplot of key trace elements of pyrite from the Zhunuo deposit.

6. Discussion

6.1. Genetic Types of Pyrite and Occurrence States of Trace Elements

The major and trace elements of pyrite, such as Co-Ni-As compositions and Co/Ni ratios, can be used to identify its genetic type [38,39]. Sedimentary pyrite typically exhibits Co/Ni < 1, whereas magmatic-hydrothermal pyrite generally shows Co/Ni > 1, and stratabound pyrite related to volcanic activity or intermediate-mafic magmatic fluids displays variable Co/Ni ratios [38,40]. Ref. [11] proposed a typomorphic formula for pyrite-major elements: $\delta S = (S - 53.45)/53.45 \times 100\%$ and $\delta Fe = (Fe - 46.55)/46.55 \times 100\%$, where δS and δFe represent the deviation percentages of S and Fe contents (wt.%) from their theoretical values respectively. The δS and δFe values of the studied samples ranged from −0.14 to 0.56 and −0.15 to 1.81, respectively, clustering predominantly in the third quadrant (magmatic-hydrothermal pyrite field) and exhibiting Fe- and S-deficient characteristics.

When arsenic in pyrite is substituted for sulfur in the form of an As^{1-} anion, a negative correlation between As and S is observed [12]. However, no correlation existed between As and S in the pyrite from the Zhunuo copper deposit (Figure 8) coupled with highly heterogeneous As contents (0.18–4323.73 μg/g), suggesting that arsenic primarily occurred as mineral inclusions. The pyrite exhibited a positive Au-As correlation, although gold concentrations were generally low (<1 ppm), except for a few samples that reached 7–10 ppm. The predominance of intergranular gold further supported arsenic occurrence as As-bearing inclusions or nanoparticles.

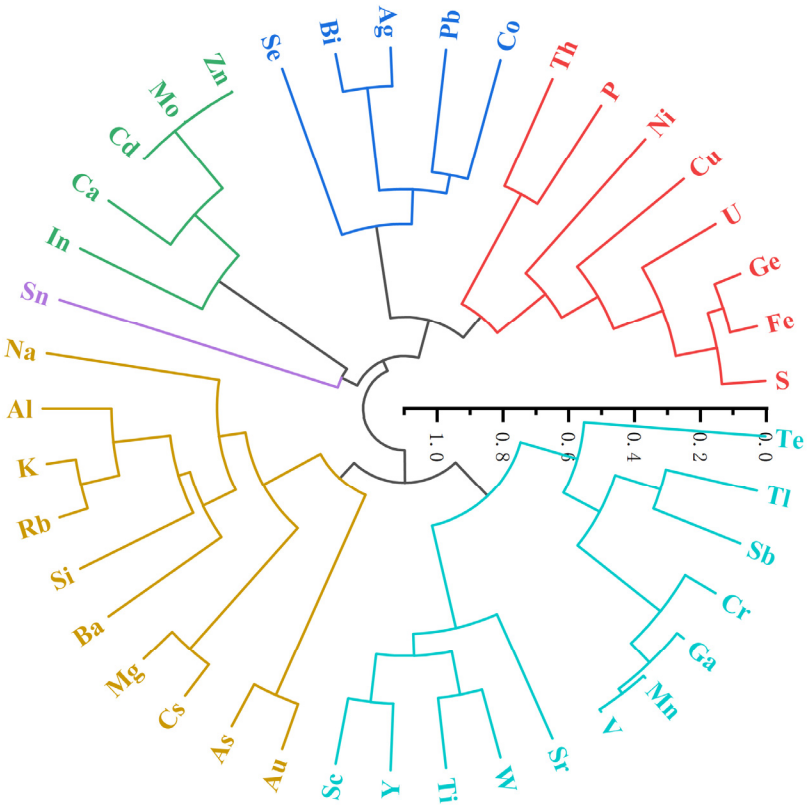


Figure 8. Circular dendrogram of a cluster analysis for pyrite from the Zhunuo copper deposit.

The absence of a Cu-Fe correlation in the Zhunuo pyrite precluded direct Cu^{2+} substitution for Fe^{2+} in the FeS_2-CuS_2 series. Copper concentrations exceeding 2000 ppm surpassed solubility limits during hydrothermal pyrite growth, indicating Cu incorporation via nano/micro-scale Cu-sulfide inclusions precipitated from Cu-saturated fluids at pyrite-fluid interfaces.

Elemental correlations (Ag-Pb-Bi, Zn-In; Figure 8) and microscopic observations of galena and sphalerite (Figure 4H) confirmed that these elements predominantly resided as mineral inclusions. The elevated Mo content in some pyrite samples was primarily attributed to the influence of molybdenite mineral inclusions during laser ablation.

6.2. Pyrite as a Record of Hydrothermal Fluid Properties

Selenium-rich pyrite typically crystallizes from low-temperature hydrothermal fluids [40,41]. A negative correlation exists between the average Se content in pyrite and the formation temperature across different deposit types. In the Zhunuo deposit, three main-stage pyrite types (Py2 and Py3) showed comparable Se concentrations (24 ± 14 ppm to 35 ± 22 ppm), while Py2 exhibited an order-of-magnitude increase (118–779 ppm). Applying the empirical thermometer $Se_{Py} = 5 \times 10^{13} \times T^{-4.82}$ (where T is in °C and Se_{Py} in ppm; [41]), we calculated formation temperatures of 372 ± 43 °C (Py2), 354 ± 48 °C (Py3), and 231 ± 30 °C (Py4). Py1 showed mostly undetected Se, but one sample reached a temperature of 480 °C. The undetected particles in the other samples could be due to the highly fragmented nature of pyrite. The Py2 and Py3 temperatures matched the fluid inclusion homogenization temperatures (340–399 °C) from quartz in the A and B veins [6]. These quartz varieties, characterized by low cathodoluminescence intensity and pore development, coexisted with Cu-Fe sulfides and showed reduced Cu/(Na + K) ratios, confirming their main mineralization-stage origin. In contrast, Py4 temperatures corresponded to D-vein quartz [6], indicating late-stage formation.

Unlike temperature-dependent Se, pyrite Te contents reflect oxygen fugacity (fO_2), with a higher Te indicating a lower fO_2 [42]. Porphyry deposits generally contain lower pyrite Te than Carlin, epithermal, or orogenic systems [41]. At Zhunuo, large Te variations (e.g., 81.87 ppm in Py2 cores vs. 7.28 ppm in rims) record dynamic fO_2 fluctuations during mineralization. In addition, the Te contents in pyrite showed significant variations across different alteration zones, indicating that Te enrichment may be independent of alteration types. Collectively, Se-Te systematics documented progressive cooling and oxidation of the Zhunuo hydrothermal system.

6.3. Pyrite Chemistry Plays a Significant Role in Porphyry-Epithermal Deposits in Xizang

Previous studies have shown that trace element contents (e.g., Te and Se) in pyrite vary significantly among different deposits [39–41]. In this study, we compared the trace element characteristics of pyrite from different deposit types in the Qinghai-Tibet Plateau. The available pyrite trace element data from four other porphyry-epithermal deposits in Tibet were compiled to further explore the implications for the genesis and exploration of porphyry-epithermal deposits. The four deposits included the Xiongcun porphyry Au-Cu deposit [27], Tiegelongnan porphyry-epithermal Cu (Au) deposit [28,43], Bada epithermal Cu-Au deposit [29], and the Xiquheqiao epithermal Cu-Au deposit [30].

In these deposits, Tiegelongnan showed the highest Cu content (Figure 9), but with a relatively low concentration of Au, As, Co, and Pb (Figure 9). This was attributed to the high-grade Cu mineralization of the Tiegelongnan deposit, which had a large part of over 0.8% Cu mineralization [43]. The Xiongcun deposit contained the lowest content of most of the studied elements, including Cu, Ni, Bi, Au, As, Ag, and Pb, except it had a relatively high Co content compared to the pyrite in other deposits (Figure 9). The pyrite from Xiongcun exhibited positive correlations between Au and Cu, Co, Ni, and As, indicating that the higher concentrations of Co, Ni, and As in pyrite corresponded to an elevated Au content [27]. However, the low abundance of these elements in Xiongcun pyrite suggest its gold-barren nature, as Au content shows a positive correlation with these elements [27], and gold is primarily partitioned into chalcopyrite instead [44]. The Bada

deposit had a relative high content of Ni, Co, Bi, As, and Ag, and As was the highest compared with the other deposits (Figure 9). This could be due to the high As in the epithermal system [45,46]. The pyrite in the Xiquheqiao deposit had the highest Au content among these deposits, and relatively high As and Pb contents. In this deposit, As entered pyrite through isomorphic substitution, while Pb was incorporated into pyrite as nano- to micron-scale particulate minerals [30]. The migration, enrichment, and precipitation of Au were closely associated with As. The adsorption of Au by As-bearing pyrite and the high degree of As isomorphism (leading to destabilization of complexes) might be the primary factors controlling Au enrichment and precipitation in this deposit [30]. Compared to the data from the literature, the Zhunuo deposit had the highest Co, Bi, Ag, and Pb contents. These elements exhibited significant clustering (Figure 8). This phenomenon was associated with the frequent occurrence of galena mineral inclusions in pyrite from the Juno copper deposit (Figure 4D).

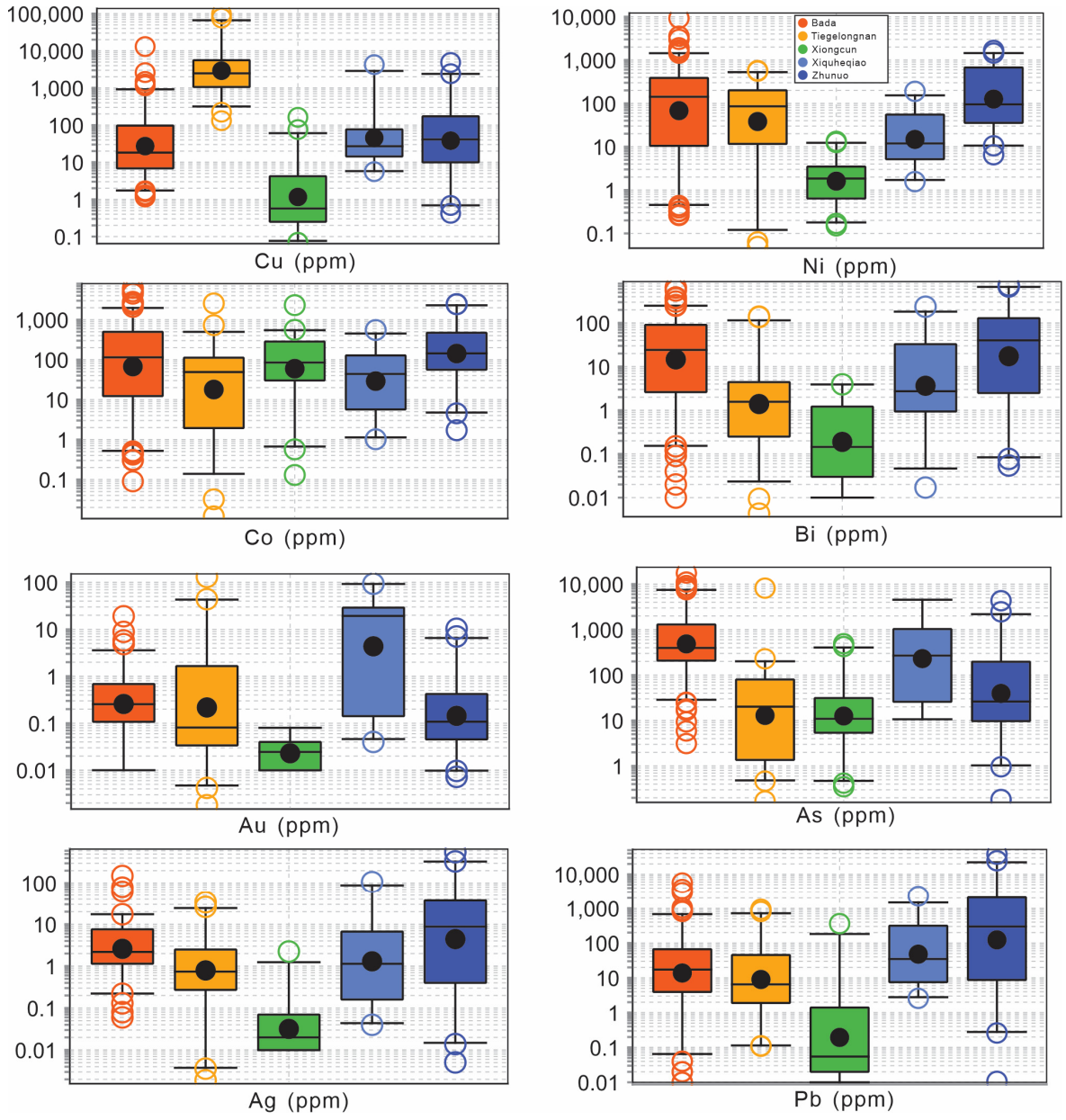


Figure 9. Box-whisker diagrams for a comparison of the pyrite trace elements from several porphyry deposits in Tibet. The box-whisker information is the same as in Figure 6.

In all these deposits, Au and As showed a positive correlation (Figure 10A), similar to that found at Zhunuo (Figure 7A), as well as in many other hydrothermal deposits [11,12,39,41]. In these deposits, Au also showed a positive correlation with Ag, although the correlation was not obvious in the samples from Xiquheqiao (Figure 10B). This might be attributed to the fact that deposits such as Xiongcun, Zhunuo, and Tiegelongnan are all associated with Ag, whereas the Xiquheqiao deposit lacks silver mineralization. Ag also shows a positive correlation with Pb and Bi as well (Figures 10C and 11D). The Xiongcun pyrite data are plotted at the lower concentration end, while Zhunuo pyrite data are located at the higher content end. Co and Ni mostly show a positive correlation in pyrite, but not for the Xiongcun pyrite, which instead had a negative correlation (Figure 10E).

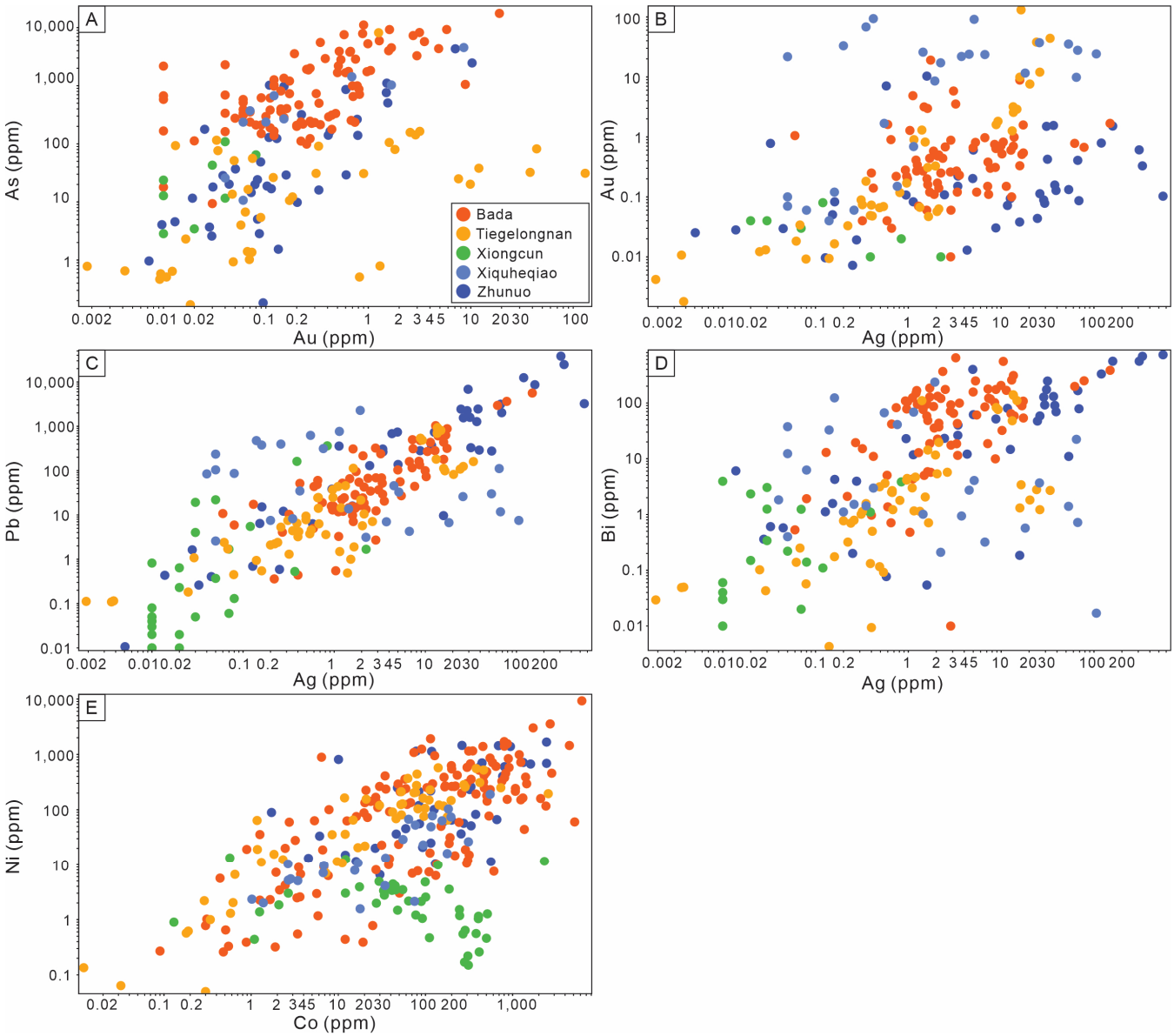


Figure 10. Biplot of key elements of pyrite from several different porphyry deposits in Tibet.

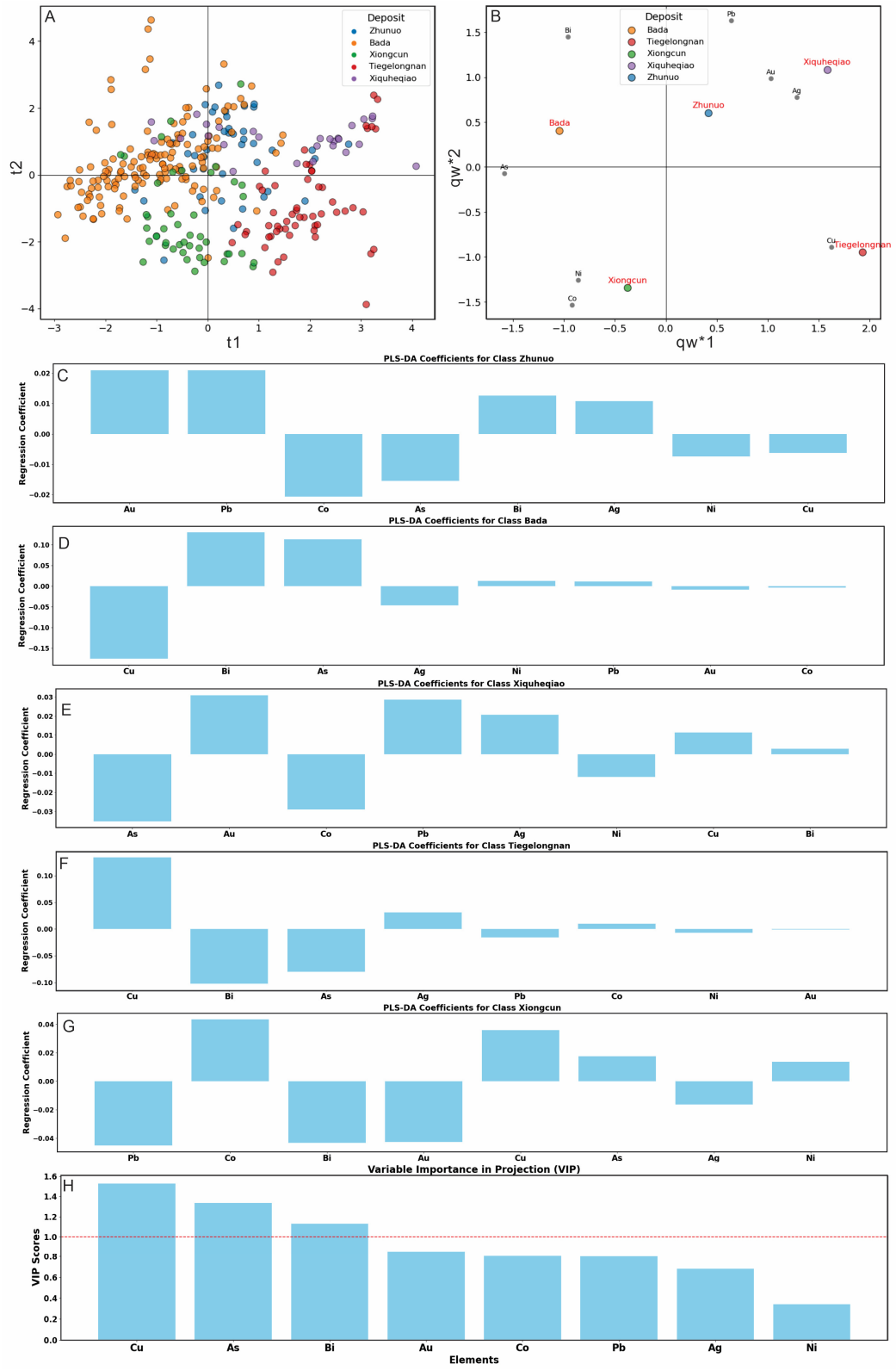


Figure 11. PLS-DA discrimination of pyrite from different porphyry deposits in Tibet. (**A**) The Score scatter plot of component t1 and t2 (first and second scores) plot showing the distribution of pyrite analysis from different deposit. (**B**) The qw*1 and qw*2 (first and second loading) plot showing correlations among elements and depositsLoading plot of component 1 and 2. (**C**–**G**) Regression coefficients of pyrite from each deposit, showing the contribution value of each element to the discrimination of each deposit. (**H**) Variable Importance in Projection (VIP) Score of selected trace elements, to quantify the importance of each element that contribute to the discrimination.

A biplot simply shows the relationship between two elements; however, the incorporation of elements into pyrite is usually more complicated and several elements may be incorporated simultaneously. As shown in Figure 10, Ag has a positive correlation with multiple elements including Au, Pb, and Bi. PLS-DA, as a multivariate statistic, can reveal the relationships between multiple elements. The PLS-DA diagram shows that it could discriminate pyrite from deposits well based on their various geochemical signatures (Figure 11). The Zhunuo pyrite data are plotted in the top-right quadrants of the score plot (Figure 11A), due to its close relationship to Bi, Pb, Au, and Ag (Figure 11B), which is consistent with the box-whisker plot suggesting Zhunuo pyrite has a relatively high content of Bi, Ag, Pb, and Au. The Xiquheqiao pyrite data were also plotted near the Zhunuo samples (Figure 11A), due to the close relationship with Pb, Au, Ag, and Bi. The Tiegelongnan deposit pyrite data were mostly plotted in the right and low quadrant (Figure 11A), due to the close relationship with Cu (Figure 11B), as suggested by the high Cu content in the box-whisker plot (Figure 11A). Pyrite from the Bada deposit were mostly plotted in the left quadrants (Figure 11A) because of the close correlation with As, Bi, Co, and Bi (Figure 11B), as there were high concentrations of these elements in this pyrite group. The Xiongcun pyrite data were mostly in the lower-left quadrant (Figure 11A), because of its high concentration of Co. Although Xiongcun data were also close to Ni (Figure 11), the VIP plot suggests that the Ni was low, thus it was not the most important discriminative element. Cu, As, and Bi had high VIP scores (Figure 11C), which suggest they are the most important elements for discriminating pyrite within these deposits. Therefore, the pyrite from the Xiongcun island-arc-type porphyry Cu-Au deposit in the Tibetan Plateau had the lowest Cu and Bi contents, while the pyrite from the Tiegelongnan continental margin arc-type porphyry-epithermal Cu-Au deposit exhibited the highest Cu content. In contrast, pyrite from collision-type porphyry and epithermal deposits showed intermediate amounts of Cu and Bi. The As content in pyrite from both island-arc and continental margin arc-type porphyry metallogenic systems was similar but lower than that found in deposits formed in post-collisional settings. Thus, As, Cu, and Bi can serve as discriminative indicators for different deposit types and metallogenic environments in the Tibetan Plateau. However, the compositional differences of pyrite in different deposits may also be controlled by the properties of the ore-forming fluids (e.g., temperature and composition) and their evolutionary processes, as well as the physicochemical characteristics of the pyrite types.

7. Conclusions

(1) The trace-element signatures and textural analysis of pyrite types in the Zhunuo deposit revealed a magmatic-hydrothermal origin with distinct mineralization stages. Main-stage pyrite (Py2 and Py3) formed at 354–372 °C, while late-stage Py4 reflected cooler D-vein conditions (231 °C). Dynamic fO_2 fluctuations were recorded by Te variability (7–82 ppm), indicating progressive oxidation during system cooling.

(2) Comparative analysis of pyrite from regional deposits (Xiongcun, Tiegelongnan, Bada, and Xiquheqiao) identified Cu-As-Bi as key discriminators (VIP > 0.8). Post-collisional systems (Zhunuo and Xiquheqiao) exhibited intermediate Cu-Bi and elevated As, contrasted with arc-related deposits. Zhunuo pyrite was uniquely enriched in Co-Bi-Ag-Pb, while Tiegelongnan showed high Cu but low Au-As, and Xiquheqiao displayed strong Au-As coupling.

(3) The study established pyrite trace-element proxies (e.g., As-Bi-Pb for Zhunuo, Se/Te for temperature, and Cu/As ratios) to reconstruct fluid evolution and distinguish porphyry-epithermal systems in collisional settings. These mineral-chemical indicators enhanced targeting strategies for Cu-Au mineralization in the Qinghai-Tibet Plateau.

Supplementary Materials: The following supporting information can be downloaded at: https://www.mdpi.com/article/10.3390/min15111113/s1, Table S1: The mineral—chemical characteristics of pyrite from different deposits in the Qinghai—Tibet Plateau; Table S2: The uncertainty of LA-ICP-MS in situ analysis of pyrite (1 Sigma) and The detection limit of LA-ICP-MS in situ analysis of pyrite.

Author Contributions: Conceptualization, H.G.; methodology, L.G.; software, L.G.; validation, H.G.; formal analysis, J.L.; investigation, H.G.; resources, J.L.; data curation, F.X.; writing—original draft preparation, H.G.; writing—review and editing, H.G.; visualization, F.X.; supervision, F.X.; project administration, F.X.; funding acquisition, J.L. All authors have read and agreed to the published version of the manuscript.

Funding: This research was supported by the Sichuan Provincial Foundation Youth Project (Grant number: 25QNJJ3968) and the Project of Tibet Xianglong Mining Co., Ltd. (Project No. 2508-ZC-2024-00096).

Data Availability Statement: Data are contained within the article.

Acknowledgments: Special thanks are given to the anonymous reviewers for their critical and constructive reviews.

Conflicts of Interest: Jiancuo Luosang is an employee of Tibet Zhongkai Holding Co., Ltd. Hongzhong Guan is an employee of Tibet Xianglong Mining Co., Ltd. The paper reflects the views of the scientists and not the company.

References

1. Sun, X.; Lu, Y.J.; McCuaig, T.C.; Zheng, Y.Y.; Chang, H.F.; Guo, F.; Xu, L.J. Miocene ultrapotassic, high-Mg dioritic, and adakite-like rocks from Zhunuo in Southern Tibet: Implications for mantle metasomatism and porphyry copper mineralization in collisional orogens. *J. Petrol.* **2018**, *59*, 341–386. [CrossRef]
2. Zheng, Y.Y.; Su, S.; Ci, Q.; Chen, S.Y.; Shi, S.D.; Chen, X.; Liu, P.; Li, J.Z. Metallogenic series and exploration breakthroughs of Zhunuo ore district in Xizang. *Miner. Depos.* **2024**, *43*, 1295–1315.
3. Li, M. Characteristics of Ore-Forming Fluid of the Zhunuo Porphyry Copper Deposit in the Gangdese Belt, Tibet. Master's Thesis, China University of Geoscience, Beijing, China, 2015.
4. Dai, J.; Chou, I.-M.; Pan, X.D.; Ding, J.; Huang, Y.; Yan, G.Q.; Shen, H.L. Fluid evolution of the Zhunuo porphyry Cu-Mo deposit in Gangdese Tract, Tibet, China: A fluid-inclusion investigation. *Ore Geol. Rev.* **2021**, *139*, 104484. [CrossRef]
5. Sun, X.; Hollings, P.; Lu, Y.J. Geology and origin of the Zhunuo porphyry copper deposit, Gangdese belt, southern Tibet. *Miner. Depos.* **2020**, *56*, 457–480. [CrossRef]
6. Sun, X.; Li, R.Y.; Si, X.B.; Xiao, K.; Deng, J. Timing and Mechanism of Ore Precipitation in Porphyry Cu Systems: Insight from LA-ICP-MS Analysis of Fluid Inclusions and In Situ Oxygen Isotope Analysis of Hydrothermal Quartz at Zhunuo Porphyry Cu Deposit, China. *Econ. Geol.* **2024**, *119*, 593–616. [CrossRef]
7. Mercer, C.N.; Reed, M.H.; Mercer, C.M. Time scales of porphyry Cu deposit formation: Insights from titanium diffusion in quartz. *Econ. Geol.* **2015**, *110*, 587–602. [CrossRef]
8. Li, Y.; Li, X.H.; Selby, D.; Li, J.W. Pulsed magmatic fluid release for the formation of porphyry deposits: Tracing fluid evolution in absolute time from the Tibetan Qulong Cu-Mo deposit. *Geology* **2018**, *46*, 7–10. [CrossRef]
9. Sykora, S.; Cooke, D.; Meffre, S.; Stephanov, A.S.; Gardner, K.; Scott, R.; Selley, D.; Harris, A. Evolution of Pyrite Trace Element Compositions from Porphyry-Style and Epithermal Conditions at the Lihir Gold Deposit: Implications for Ore Genesis and Mineral Processing. *Econ. Geol.* **2018**, *113*, 193–208. [CrossRef]
10. Li, H.G.; Zhang, Z.C.; Zhang, R.; Xie, Q.H.; Zhang, L.; Santosh, M. Geochemical discrimination of pyrite in diverse ore deposit types through statistical analysis and machine learning techniques. *Am. Mineral.* **2024**, *109*, 846–857. [CrossRef]
11. Yan, Y.T.; Li, S.R.; Jia, B.J.; Zhang, N.; Yan, L.N. Composition typomorphic characteristics and statistic analysis of pyrite in gold deposits of different genetic types. *Earth Sci. Front.* **2012**, *19*, 214–226.
12. Reich, M.; Deditius, A.; Chryssoulis, S.; Li, J.W.; Ma, C.Q.; Parada, M.A.; Barra, F.; Mittermayr, F. Pyrite as a record of hydrothermal fluid evolution in a porphyry copper system: A SIMS/EMPA trace element study. *Geochim. Cosmochim. Acta* **2013**, *104*, 42–62. [CrossRef]
13. Alford, L.; Gysi, A.; Hurtig, N.; Monecke, T.; Pfaff, K. Porphyry-related polymetallic Au-Ag vein deposit in the Central City district, Colorado: Mineral paragenesis and pyrite trace element chemistry. *Ore Geol. Rev.* **2020**, *119*, 103295. [CrossRef]
14. Velojic, M.; Erlandsson, V.B.; Melcher, F.; Onuk, P.; Jelenkovic, R.; Cvetkovic, V. Trace elements in pyrite from the Cukaru Peki porphyry Cu-high-sulfidation deposit, Serbia: Implications for ore evolution in a polyphase hydrothermal system. *Geol. Croat.* **2022**, *75*, 303–316. [CrossRef]

15. Xiao, X.; Zhou, T.F.; Hollings, P.; White, N.C.; Fan, Y.; Zhang, L.J.; Fu, B. Pyrite geochemistry in a porphyry-skarn Cu (Au) system and implications for ore formation and prospecting: Perspective from Xinqiao deposit, Eastern China. *Am. Mineral.* **2023**, *108*, 1132–1148. [CrossRef]
16. Yang, Z.M.; Lu, Y.J.; Hou, Z.Q.; Chang, Z.S. High-Mg diorite from Qulong in southern Tibet: Implications for the genesis of adakite-like intrusions and associated porphyry Cu deposits in collisional orogens. *J. Petrol.* **2015**, *56*, 227–254. [CrossRef]
17. Tang, J.X.; Deng, S.L.; Zheng, W.B.; Ying, L.J.; Wang, X.W.; Qin, Z.P.; Ding, F.; Li, F.J.; Tang, X.Q.; Zhong, Y.F.; et al. An exploration model for Jiama copper polymetallic deposit in Maizhokunggar County, Tibet. *Miner. Depos.* **2011**, *30*, 179–196.
18. Tang, J.X.; Lang, X.H.; Xie, F.W.; Gao, Y.M.; Li, Z.J.; Huang, Y.; Ding, F.; Yang, H.H.; Zhang, L.; Wang, Q.; et al. Geological characteristics and genesis of the Jurassic No. I porphyry Cu-Au deposit in the Xiongcun district, Gangdese porphyry copper belt, Tibet. *Ore Geol. Rev.* **2015**, *70*, 438–456. [CrossRef]
19. Zhao, X.Y.; Yang, Z.S.; Zheng, Y.C.; Liu, Y.C.; Tian, S.H.; Fu, Q. Geology and genesis of the post-collisional porphyry-skarn deposit at Bangpu, Tibet. *Ore Geol. Rev.* **2015**, *70*, 486–509. [CrossRef]
20. Zhu, D.C.; Zhao, Z.D.; Niu, Y.L.; Mo, X.X.; Chung, S.L.; Hou, Z.Q.; Wang, L.Q.; Wu, F.Y. The Lhasa Terrane: Record of a microcontinent and its histories of drift and growth. *Earth Planet. Sci. Lett.* **2011**, *301*, 241–255. [CrossRef]
21. Zhang, Z.M.; Dong, X.; Santosh, M.; Zhao, G.C. Metamorphism and tectonic evolution of the Lhasa terrane, central Tibet. *Gondwana Res.* **2014**, *25*, 170–189. [CrossRef]
22. Zhu, D.C.; Pan, G.T.; Chung, S.L.; Liao, Z.L.; Wang, L.Q.; Li, G.M. SHRIMP zircon age and geochemical constraints on the origin of Lower Jurassic volcanic rocks from the Yeba Formation, southern Gangdese, south Tibet. *Int. Geol. Rev.* **2008**, *50*, 442–471. [CrossRef]
23. Ji, W.Q.; Wu, F.Y.; Chung, S.L.; Li, J.X.; Liu, C.Z. Zircon U-Pb geochronology and Hf isotopic constraints on petrogenesis of the Gangdese batholith, southern Tibet. *Chem. Geol.* **2009**, *262*, 229–245. [CrossRef]
24. Xie, F.W.; Tang, J.X. The Late Triassic-Jurassic magmatic belt and its implications for the double subduction of the Neo-Tethys Ocean in the southern Lhasa subterrane Tibet. *Gondwana Res.* **2021**, *97*, 1–21. [CrossRef]
25. Zhu, D.C.; Li, S.M.; Cawood, P.A.; Wang, Q.; Zhao, Z.D.; Liu, S.A.; Wang, L.Q. Assembly of the Lhasa and Qiangtang terranes in central Tibet by divergent double subduction. *Lithos* **2016**, *245*, 7–17. [CrossRef]
26. Gustafson, L.B.; Hunt, J.P. The porphyry copper deposit at El Salvador, Chile. *Econ. Geol.* **1975**, *70*, 857–912. [CrossRef]
27. Wu, C.Y.; Lang, X.H.; Zhang, H.; Wang, X.H.; Zhang, P.; Deng, Y.L.; Lou, Y.M.; Jiang, K. Typomorphic characteristics and geological significance of pyrite from No. 1 deposit in the Xiongcun district, Tibet. *Bull. Mineral. Petrol. Geochem.* **2024**, *43*, 372–386. [CrossRef]
28. Zhang, Q.; Chen, W.; Yang, H.H.; Fu, X.L.; Wang, Q.; Li, Y.B.; Li, H.W.; Xin, T.; Liang, X.J.; Li, S.; et al. Characteristic and Significance of Pyrite at Tiegelongnan Cu (Au) Deposit, Duolong Ore District, Tibet. *Acta Geosci. Sin.* **2023**, *44*, 983–999.
29. Wu, H.; Zhu, X.P.; Jia, Q.; Zhang, B.; Li, Y.; Yang, L.C. Characteristics and environmental effects of in situ major and trace elements in pyrite from the Bada copper-gold deposit in Tibet. *Acta Geol. Sin.* **2023**, *97*, 2261–2280.
30. Bai, A.D.; Li, B.; Tang, G.; Wang, X.F.; Shu, H.W.; Yue, Y.; Li, Y.B. In situ trace element and sulfur isotopic compositions of pyrites from the Xiquheqiao copper-gold deposit, Mangkang County, Xizang, China. *Acta Mineral. Sin.* **2025**, *45*, 146–159. [CrossRef]
31. Makvandi, S.; Ghasemzadeh-Barvarz, M.; Beaudoin, G.; Grunsky, E.C.; McClenaghan, M.B.; Duchesne, C.; Boutroy, E. Partial least squares-discriminant analysis of trace element compositions of magnetite from various VMS deposit subtypes: Application to mineral exploration. *Ore Geol. Rev.* **2016**, *78*, 388–408. [CrossRef]
32. Huang, X.W.; Sappin, A.A.; Boutroy, E.; Beaudoin, G.; Makvandi, S. Trace Element Composition of Igneous and Hydrothermal Magnetite from Porphyry Deposits: Relationship to Deposit Subtypes and Magmatic Affinity. *Econ. Geol.* **2019**, *114*, 917–952. [CrossRef]
33. Makvandi, S.; Huang, X.W.; Beaudoin, G.; Quirt, D.; Ledru, P.; Fayek, M. Trace element signatures in hematite and goethite associated with the Kiggavik-Andrew Lake structural trend U deposits (Nunavut, Canada). *Miner. Depos.* **2021**, *56*, 509–535. [CrossRef]
34. Liu, H.M.; Beaudoin, G.; Makvandi, S.; Jackson, S.E.; Huang, X.W. Multivariate statistical analysis of trace element compositions of native gold from orogenic gold deposits: Implication for mineral exploration. *Ore Geol. Rev.* **2021**, *131*, 104061. [CrossRef]
35. Caraballo, E.; Dare, S.; Beaudoin, G. Variation of trace elements in chalcopyrite from worldwide Ni-Cu sulfide and Reef-type PGE deposits: Implications for mineral exploration. *Miner. Depos.* **2022**, *57*, 1293–1321. [CrossRef]
36. Miranda, A.C.R.; Beaudoin, G.; Rottier, B. Scheelite chemistry from skarn systems: Implications for ore-forming processes and mineral exploration. *Miner. Depos.* **2022**, *57*, 1469–1497. [CrossRef]
37. Egozcue, J.J.; Pawlowsky-Glahn, V.; Mateu-Figueras, G.; Barceló-Vidal, C. Isometric Logratio Transformations for Compositional Data Analysis. *Math. Geol.* **2003**, *35*, 279–300. [CrossRef]
38. Brill, B.A. Trace-element contents and partitioning of elements in ore minerals from the CSA Cu-Pb-Zn deposit, Australia. *Can. Mineral.* **1989**, *27*, 263–274.

39. Large, R.R.; Danyushevsky, L.V.; Hollit, C.; Maslennikov, V.; Meffre, S.; Gilbert, S.E.; Bull, S.; Scott, R.J.; Emsbo, P.; Thomas, H.; et al. Gold and trace element zonation in pyrite using a laser imaging technique: Implications of the timing of gold in orogenic and Carlin-style sediment-hosted deposits. *Econ. Geol.* **2009**, *104*, 635–668. [CrossRef]
40. Zhao, Z. *Principles of Trace Element Geochemistry*, 2nd ed.; Science Press: Beijing, China, 2016. (In Chinese)
41. Keith, M.; Haase, K.M.; Chivas, A.R.; Klemd, R. Phase separation and fluid mixing revealed by trace element signatures in pyrite from porphyry systems. *Geochim. Cosmochim. Acta* **2022**, *329*, 185–205. [CrossRef]
42. Gao, S.; Xu, H.; Li, S.X.; Santosh, M.; Zhang, D.; Yang, L.; Quan, S. Hydrothermal alteration and ore-forming fluids associated with gold-tellurium mineralization in the Dongping gold deposit, China. *Ore Geol. Rev.* **2017**, *80*, 166–184. [CrossRef]
43. Yang, C.; Beaudoin, G.; Tang, J.-X.; Song, Y.; Wang, L.-Q.; Huang, X.-W. Cu-sulfide mineralogy, texture, and geochemistry in the Tiegelongnan porphyry-epithermal copper system, Tibet, China. *Miner. Depos.* **2022**, *57*, 759–779. [CrossRef]
44. Simon, G.; Kesler, S.E.; Essense, E.J.; Chryssoulis, S.L. Gold in porphyry copper deposits: Experimental determination of the distribution of gold in the Cu-Fe-S system at 400° to 700 °C. *Econ. Geol.* **2000**, *95*, 259–270. [CrossRef]
45. White, N.C.; Hedenquist, J.W. Epithermal gold deposits: Styles, characteristics and exploration. *SEG Newsl.* **1995**, *23*, 9–13. [CrossRef]
46. Simmons, S.F.; Brown, K.L.; Tutolo, B.M. Hydrothermal transport of Ag, Au, Cu, Pb, Te, Zn, and other metals and metalloids in New Zealand geothermal systems: Spatial patterns, fluid-mineral equilibria, and implications for epithermal mineralization. *Econ. Geol.* **2016**, *111*, 589–618. [CrossRef]

Disclaimer/Publisher's Note: The statements, opinions and data contained in all publications are solely those of the individual author(s) and contributor(s) and not of MDPI and/or the editor(s). MDPI and/or the editor(s) disclaim responsibility for any injury to people or property resulting from any ideas, methods, instructions or products referred to in the content.